Targeted Nanoparticles with High Heating Efficiency for the Treatment of Endometriosis with Systemically Delivered Magnetic Hyperthermia

Youngrong Park,

Ananiya A Demessie

College of Pharmacy, Oregon State University, 2730 SW Moody Avenue, Portland, Oregon 97201, USA

Addie Luo

Division of Reproductive and Developmental Sciences, Oregon National Primate Research Center, Oregon Health & Science University, 505 NW 185th Avenue Beaverton, Oregon 97006, USA

Olena R Taratula,

Abraham S Moses,

Peter Do

College of Pharmacy, Oregon State University, 2730 SW Moody Avenue, Portland, Oregon 97201, USA

Leonardo Campos,

Younes Jahangiri

Dotter Interventional Institute, Department of Interventional Radiology, Oregon Health & Science University, 3181 SW Sam Jackson Park Road, Portland, Oregon 97239, USA

Cory R. Wyatt,

Department of Diagnostic Radiology, Oregon Health & Sciences University, 3181 SW Sam Jackson Park Road, Portland, Oregon 97239, USA

Advanced Imaging Research Center, Oregon Health & Sciences University, 3181 SW Sam Jackson Park Road, Portland, Oregon 97239, USA

Hassan A. Albarqi,

Department of Pharmaceutics, College of Pharmacy, Najran University, King Abdulaziz Road, Najran 55461, Kingdom of Saudia Arabia

Khashayar Farsad,

Dotter Interventional Institute, Department of Interventional Radiology, Oregon Health & Science University, 3181 SW Sam Jackson Park Road, Portland, Oregon 97239, USA

Ov D Slayden,

Division of Reproductive and Developmental Sciences, Oregon National Primate Research Center, Oregon Health & Science University, 505 NW 185th Avenue Beaverton, Oregon 97006, USA

Oleh Taratula

College of Pharmacy, Oregon State University, 2730 SW Moody Avenue, Portland, Oregon 97201, USA

Abstract

Endometriosis is a devastating disease in which endometrial-like tissue forms lesions outside the uterus. It causes infertility and severe pelvic pain in ~176 million women worldwide, and there is currently no cure for this disease. Magnetic hyperthermia could potentially eliminate widespread endometriotic lesions but has not previously been considered for treatment because conventional magnetic nanoparticles have relatively low heating efficiency and can only provide ablation temperatures (>46 °C) following direct intralesional injection. This study is the first to describe nanoparticles that enable systemically delivered magnetic hyperthermia for endometriosis treatment. When subjected to an alternating magnetic field (AMF), these hexagonal iron-oxide nanoparticles exhibit extraordinary heating efficiency that is 6.4 times greater than their spherical counterparts. Modifying nanoparticles with a peptide targeted to vascular endothelial growth factor receptor 2 enhances their endometriosis specificity. Studies in mice bearing transplants of macaque endometriotic tissue revealed that, following intravenous injection at a low dose (3 mg per kg), these nanoparticles efficiently accumulate in endometriotic lesions, selectively elevate intralesional temperature above 50 °C upon exposure to external AMF, and completely eradicate them with a single treatment. These nanoparticles also demonstrate promising potential as MRI contrast agents for precise detection of endometriotic tissue before AMF application.

Graphical Abstract
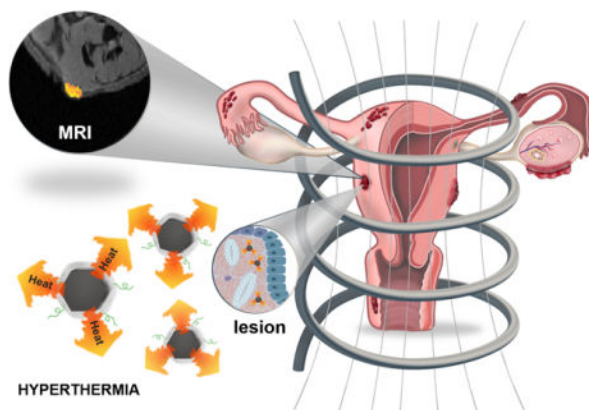
Endometriosis is a debilitating systemic disease in which tissue that resembles the uterine lining (the endometrium) forms vascularized lesions outside the uterus, often disseminating to distal sites. Novel endometriosis-targeted hexagonal nanoparticles efficiently accumulate in these lesions following systemic administration, enabling improved detection with MRI. Upon exposure to an external alternating magnetic field, nanoparticles generate heat within lesions, completely eliminating them.

Keywords

nanoparticles; magnetic hyperthermia; MRI; endometriosis; targeting peptide

1. Introduction

Endometriosis is a debilitating systemic disease in which tissue that resembles the uterine lining (the endometrium) grows outside the uterus.[1–3] It causes infertility and severe pelvic pain in approximately 176 million women worldwide.[3] Although endometriosis is a non-malignant disorder, lesions, in some cases, can perforate the underlying organs, resulting in a potentially fatal condition.[2] Despite recent advances in the treatment of endometriosis-related pain, this disease still has no cure.[1,4] All approved medical therapies result in infertility, and patients who want to improve their fertility frequently seek surgical excision of the lesions.[1,5,6] Unfortunately, the recurrence rate after surgery is high, with 27% of patients requiring multiple surgical procedures.[7] Moreover, complications that can occur during and after surgery contribute to overall risks. Therefore, the need for an efficient non-surgical method of removing the lesions is urgent.

Nanoparticle-mediated magnetic hyperthermia is a clinical intervention to treat cancerous tissue by increasing the temperature of tumors.[8–12] The rationale for employing magnetic hyperthermia in cancer treatment is well established in preclinical and clinical studies. [9–16] This approach is built on rigorous prior research showing the ability of magnetic nanoparticles to generate heat in the presence of an alternating magnetic field (AMF). [8,13] After the delivery of the nanoparticles into tumors, exposure to external AMF remotely elevates intratumoral temperature while minimizing the exposure of organs to tissue-destructive heat.[16,17] Heating tumors above 42 °C can result in cell death via apoptosis (42 – 46 °C) or necrosis (> 46 °C, thermoablation).[17,18] Previous reports reveal that intratumoral temperatures below 45 °C only inhibit tumor growth.[19,20] Intratumoral temperatures above 46 °C, on the other hand, can completely eradicate cancer tissue.[13]

Magnetic hyperthermia has not been explored as an alternative therapy for endometriosis. Our premise is that it can be used as a targeted non-surgical therapy to eradicate endometriotic lesions. This premise emanates from our previous reports, which revealed that the nanoparticles preferentially accumulated in the endometriotic grafts after intravenous (IV) injection.[21,22] This biodistribution is due to the fact that endometriosis, like cancer, is an angiogenesis-dependent disease, and the long-circulating nanoparticles can extravasate into endometriotic lesions through their fenestrated blood vessels.[21–23] Our studies also demonstrated the therapeutic effect of hyperthermia generated by photothermal therapy on macaque endometriotic lesions engrafted in mice. The grafts were eradicated after exposure to 47 °C, with no recurrence.[22] The reported photothermal therapy has significant potential for the treatment of endometriosis only during surgery because near-infrared (NIR) light, needed for activation of a photoactive agent, has limited tissue penetration (1 – 1.5 cm). [24] The AMF required for the heating of nanoparticles during magnetic hyperthermia can overcome this issue. Clinical studies reveal that the AMF generated by a human applicator (NanoActivator®) is safe and produces hyperthermia (> 42 °C) in deep-seated tumors

(e.g., glioblastoma, prostate) directly injected with nanoparticles.[10–12] The AMF used for hyperthermia is well tolerated and does not impact physiological processes in humans and large animals.[10–12,25,26]

Presently, magnetic hyperthermia is used to treat accessible malignant tumors because required temperatures (> 42 °C) have only been reached after intratumoral administration of currently used magnetic nanoparticles.[8–12] This limitation is associated with the low heating efficiency of the conventional nanoparticles combined with their low tumor accumulation after systemic delivery. Recent reports highlighted the difficulties involved with raising intratumoral temperatures above 38 °C after IV injection of iron oxide nanoparticles at clinically relevant doses (< 10 mg per kg).[27–29] The recommended dose of magnetic iron oxide nanoparticles (ferumoxytol) approved by the FDA is 510 mg (< 10 mg per kg).[30] To fully exploit the therapeutic potential of magnetic hyperthermia, it is crucial to design nanoparticles with high heating efficiency that can effectively accumulate in disease tissues after a single IV injection at clinically relevant doses (< 10 mg per kg) and generate high intratumoral and intralesional temperatures (> 46 °C) in the presence of AMF required for complete eradication of endometriosis and cancer tissues. There have been attempts to improve the heating efficiency of conventional iron oxide nanoparticles by changing various parameters, including size, shape, and core composition.[18,27,31–36] These studies revealed that heating efficiency achieved in vitro cannot always be translated into the required intratumoral heating after systemic nanoparticle administration.[18,27,32,33]

Herein, we report for the first time biocompatible magnetic nanoparticles capable of efficient accumulation in endometriotic xenografts after one IV administration at a clinically relevant dose (3 mg per kg) and generation of the required ablation temperatures (> 50 °C) in these lesions upon exposure to AMF. The xenografts were completely eradicated after a single 20-minute session of systemically delivered magnetic hyperthermia. Furthermore, our results confirmed the efficiency of the developed nanoparticles as a T2-weighted magnetic resonance imaging (MRI) contrast agent. This feature of the nanoparticles can allow their visualization in endometriotic lesions by MRI and target the focused AMF to the lesions, preventing the potential heating of normal tissues containing nanoparticles.

2. Results and Discussion

2.1. Development of magnetic nanoparticles with high heating efficiency

A modified thermal decomposition approach was developed to synthesize novel iron oxide-based magnetic nanoparticles (MN) with high heating efficiency.[20] Transmission electron microscopy (TEM) analysis revealed that MN have an irregular hexagonal shape, and the size is 18.9 ± 1.8 nm (Figure 1a). The size of MN was obtained by measuring the maximum distance between two opposite vertices of an irregular hexagon (Figure 1a inset).

We synthesized hexagonal iron oxide nanoparticles because previous reports suggest that nanoparticles with non-spherical shapes exhibit superior heating ability than spherical ones. [37] We also doped hexagonal iron oxide nanoparticles during the synthetic procedure with a small amount of cobalt (Co), enhancing their heating efficiency.[20] Energy dispersive X-ray (EDX) analysis revealed that synthesized MN contain ~1.3% Co, 34.8% Fe and 63.9% O.

Our measurements (Figure 1c) demonstrated that the heating efficiency of the synthesized hexagonal MN (specific absorption rate (SAR) = 8057 W g^{-1}) subjected to AMF was 6.4 times higher than spherical iron oxide nanoparticles (SAR = 1254 W g^{-1}) with a comparable size 19.5 ± 1.9 nm (Figure 1b).

To transfer hydrophobic MN coated with oleic acid to an aqueous phase, we encapsulated them into poly(ethylene glycol)-*block*-poly(ε-caprolactone) (PEG-PCL)-based nanocarriers by using the solvent evaporation method (Figure 2a).[22,38] PEG-PCL based nanocarriers are promising vehicles for systemic delivery of therapeutic and imaging agents due to high biocompatibility, long-circulation, and ease of conjugation by versatile coupling strategies. [38,39] Cryo-TEM images show that MN are individually coated by PEG-PCL polymer, and the thickness of the PEG-PCL layer is 3.6 nm (Figure 2b). Dynamic light scattering (DLS) analysis (Figure 2c) further demonstrates that PEG-PCL-coated MN have a hydrodynamic diameter of 30.5 ± 11.1 nm (polydispersity index (PDI) = 0.14), and a slightly negative surface charge (−1.31 ± 0.19 mV). Our previous report reveals that after intravenous injection, dye-loaded polymeric nanoparticles with similar parameters efficiently accumulate in endometriotic grafts via passive targeting.[22]

2.2. Preparation of endometriosis-targeted magnetic nanoparticles

To enhance the accumulation and specificity of the PEG-PCL-coated MN for endometriotic cells, we modified their surfaces with peptides to target vascular endothelial growth factor receptor 2 (also known as KDR), which is overexpressed in endometriotic cells and minimally expressed or temporally restricted in other tissues.[40] We employed a heptapeptide *(ATWLPPR)* VEGFR/KDR antagonist as a targeting ligand, demonstrating a high affinity for the KDR receptor.[41] In the first step, carboxylic acid-terminated PEG-PCL was conjugated to this peptide by coupling the carboxylic group of PEG to the terminal amine group in the peptide sequence (Figure 2e). A quantitative fluorometric peptide assay validated that the KDR peptide was conjugated to the PEG-PCL polymer. In the second step, a mixture of the synthesized peptide-PEG-PCL and methoxy terminated PEG-PCL (CH_3O-PEG-PCL), used for the preparation of non-modified nanoparticles (Figure 2a, b), was employed at ratio 1:9 to prepare KDR-targeted MN (KDR-MN, Figure 2f). DLS analysis revealed that an average hydrodynamic diameter of KDR-MN (33.5 ± 13.6 nm, PDI = 0.14) was 3 nm larger than non-targeted MN (30.5 ± 11.1 nm, PDI = 0.14) (Figure 2c). Zeta potential measurements demonstrated that KDR-targeted MN (−1.47 ± 0.32 mV) and non-targeted MN (−1.31 ± 0.19 mV) have a slightly negative charge. Finally, cryo-TEM images indicate that KDR-MN are also individually coated by PEG-PCL polymer and the thickness of the PEG-PCL layer is similar to the non-targeted MN (Figure 2d). The heating profile of KDR-MN suggests that PEG-PCL coating decreases the heating rate of MN, but not the maximum temperature generated by these nanoparticles in an aqueous solution. After exposure to AMF, non-coated MN (Fe concentration =1.0 mg mL^{-1}) increases the temperature of THF solution up to 72.9 °C within 30 seconds. In contrast, KDR-MN dispersed in aqueous solution (1.0 mg mL^{-1}) cross the 72.9 °C threshold in 283 seconds, reaching a maximum temperature of 100.3 °C in 600 seconds (Figure S1). According to the literature, the decrease in the heating rate of PEG-PCL-coated MN could be attributed to nanoparticle surface modification and an increase in the solvent viscosity

(THF: 0.48 cP and water: 0.89 cP at 25 °C).[20,42] Our previous report indicates that the self-assembled structure of PEG-PCL-based nanocarriers is compromised in the intracellular environment of endometriosis cells, resulting in the release of hydrophobic cargos.[22] Given that our confocal microscopy studies validate that endometriosis cells internalize KDR-MN nanoparticles (Figure S2–S3), it is reasonable to assume that hydrophobic MN would be released from PEG-PCL carriers following accumulation in endometriosis lesions, minimizing the effect of the PEG-PCL coating on the MN heating rate. We also demonstrated that a minimum concentration of PEG-PCL-coated MN of 0.19 mg Fe per mL is required to reach 46 °C in an aqueous solution within 20 minutes (Figure S4).

2.3. In vitro evaluation of cellular uptake, heating and therapeutic efficiency of non-targeted and KDR-targeted MN

The KDR receptor plays a pivotal role in the neovascularization of endometriosis.[43] Previous reports and our results suggest that KDR expression levels are significantly higher in both human and macaque endometriosis lesions when compared to the inner lining of the uterus (eutopic endometrium) (Figure 3).[44] It was also reported that there is no significant difference in KDR levels in the inner lining of the uterus between patients with endometriosis and healthy women.[45] KDR expression is minimal in the inner lining of the uterus except during the early follicular phase, a period called the luteal follicular transition associated with menstruation.[46]

Hormonal regulation of KDR has been reported in eutopic endometrium of women[47] and macaques.[48] KDR expression is elevated in the early proliferative phase and decreased by progesterone in the secretory phase. We also confirmed that KDR expression in the inner lining of the uterus of macaques is elevated in the proliferative phase compared to the secretory phase (Figure 3a,c,e). However, KDR levels in endometriosis lesions are significantly higher during both the proliferative and secretory phases than in the eutopic endometrium during the proliferative phase, when KDR expression in the eutopic endometrium is elevated due to hormonal regulation. Figure 3e reveals that KDR levels in macaque endometriosis lesions are ~10 times higher than eutopic endometrium tissue in the secretory phase. As a result, our treatment can potentially be used during both phases, as KDR levels in endometriosis lesions are always higher than those in the inner lining of the uterus. Moreover, treatment with KDR-targeted nanoparticles in the late to mid-luteal phase will minimize potential off-target effects on the inner lining of the uterus because KDR expression in this tissue is reduced. Our data also validate that KDR receptors are significantly overexpressed in endometriosis relative to organ tissues (e.g., kidney) (Figure. 3e).

Our developed nanoparticles can also be chemically modified with other ligands targeting overexpressed receptors on endometriosis cells, including CD44,[49] EphB4,[23] CXCL13,[50] CTLA4,[51] and CD10.[52] For example, reports indicate that CD44 and EphB4 receptors are overexpressed in endometriotic cells, and nanoparticles modified with targeting moieties to these receptors (hyaluronic acid and TNYL peptide) show substantially higher accumulation in endometriotic lesions when compared to their non-targeted counterparts. [23,49]

To evaluate the ability of KDR peptides to enhance the internalization efficiency of MN into cells overexpressing KDR receptors, primary cells were isolated from macaque endometriosis lesions, eutopic endometrium and kidneys. qPCR (quantitative polymerase chain reaction) analysis validates significantly higher KDR mRNA expression in cells isolated from macaque endometriotic lesions when compared to cells of normal endometrium and kidney cells (Figure S5). Cultured cells were treated with non-targeted and KDR-targeted MN loaded with a fluorescent dye (Nile Red) for 24 hours and analyzed with flow cytometry. Flow cytometry results reveal that KDR peptide significantly enhances nanoparticle binding to macaque endometriosis stromal cells but not to endometrium and kidney cells (Figure 4a). The mean fluorescent intensity of endometriosis cells treated with KDR-targeted MN was 2.5 times higher when compared to non-modified nanoparticles (Figure 4a).

Z-stack confocal microscopy images suggest that both non-targeted and KDR-targeted MN are internalized by endometriosis cells (Figure S2). Furthermore, the fluorescence intensity in cells treated with KDR-targeted MN was significantly higher than that of cells treated with non-targeted nanoparticles (Figure S3).

To evaluate the therapeutic and heating efficiency of both non-targeted and KDR-targeted MN in vitro, pellets of macaque endometriosis cells incubated with the tested nanoparticles as described above were subjected to AMF. Temperature was measured during AMF exposure using a fiber optic thermal probe placed inside the pellets. The obtained temperature profiles revealed that due to the enhanced cellular uptake, KDR-MN exhibit superior cellular heating efficiency in the presence of AMF than non-modified nanoparticles (Figure. 4b). KDR-targeted MN increased cellular temperature from 37 °C to 52.6 °C, reaching 46 °C inside the cell pellets within 340 seconds. In contrast, non-targeted nanoparticles raised the temperature of the cell pellets only up to 51.1 °C, reaching 46 °C within 520 seconds under the same experimental conditions. Magnetic hyperthermia mediated by the non-targeted and KDR-MN decreased the viability of macaque endometriosis cells by 85% and 93%, respectively (Figure. 4c). Of note, AMF exposure of cells only (without nanoparticles) resulted in minimal temperature changes and cell death (Figure. 4b, c). The difference in cell viability following magnetic hyperthermia mediated by non-targeted and KDR-targeted MN could be explained by the fact that cells treated with KDR-MN were exposed to temperatures above 46 °C for a longer duration (24 minutes) than cells treated with non-targeted MN (21 minutes, Figure 4b). Moreover, KDR-MN increased cellular temperature to 52.6 °C, whereas non-targeted nanoparticles only raised the temperature of the cell pellets to 51.1 °C. Finally, cells incubated with KDR-MN were subjected to higher temperatures during the 30 minutes of AMF exposure than cells treated with non-targeted MN (Figure. 4b).

2.4.   Endometriosis mouse model

The capacity for human and nonhuman primate tissues to grow in vivo in chimeric models of experimental endometriosis has proven to be useful for preclinical testing of novel therapies.[53,54] Several laboratories, including ours, have demonstrated that human and macaque endometrium, as well as ectopic endometriosis, can be transplanted into

immunocompromised mice.[55] Mouse strains previously employed for this purpose include athymic (nude) mice, Severe Combined Immunodeficient (SCID) mice, SCID beige mice and transgenic RAG-2 null (Recombinant Activating Gene 2/ rag2 null; Rag 2 null common cytokine receptor γ chain (γc) double null) mice. These mice lack a fully competent immune system with varying degrees of immunodeficiency associated with reduced or absent populations of lymphocytes and, therefore, do not mount an immune response to endometrium and endometriosis xenografts.[56,57] Experimental endometriosis can be created using tissues obtained from subjects with and without endometriosis via endometrial biopsy, the collection of menstrual effluent, or from laparoscopic surgical specimens. In each of these cases, the resulting grafts display endometriotic stroma and glands similar to the clinical disease in women.[21,22,58] Our studies have employed a model where rhesus macaque endometrium (or ectopic endometriosis) is engrafted into SCID mice. To induce cyclic growth of the engrafted primate tissues, the mice are treated with hormone-releasing pellets that produce human levels of estradiol (E2) and progesterone (P4).[59] In a typical experiment, mice are engrafted with endometrium or endometriotic tissue and treated with E2 (90-day release) and P4 (14-day release). As P4 levels decline, the tissues undergo a bleeding event similar to menstruation.[58] This is followed by renewed angiogenesis similar to endometriotic lesions in women and nonhuman primates.[60] The xenografts are then allowed to grow for an additional 4–6 weeks with replacement of P4-releasing pellets before further studies. This artificial cycle treatment reduces the effect of the initial graft surgery and acute inflammation on study outcomes.

2.5. In vivo evaluation of nanoparticle-mediated magnetic hyperthermia

To validate that our targeted nanoparticles efficiently accumulate in endometriotic lesions following systemic administration, mice bearing multiple grafts (Figure 5a) were IV injected with KDR-MN (3 mg Fe per kg) loaded with a NIR fluorescence dye (SiNc). The acquired images of mice revealed that a strong SiNc-generated NIR fluorescence signal is present in all endometriotic grafts (Figure 5a). To further confirm that PEG-PCL-based polymeric vehicles also delivered the prepared iron oxide-based MN, endometriotic grafts were dissected and stained with Prussian blue used to detect iron. As shown in Figure 5b, Prussian blue staining is distributed throughout the endometriosis tissue from the edge to the center. These results demonstrate that systemically injected KDR-MN can efficiently reach the periphery of endometriotic grafts via passive targeting and penetrating their cores. The observed distribution of KDR-MN is an important criterion for homogeneous heating of endometriotic lesions and their efficient eradication. It has been widely recognized that the heterogeneous nanoparticle distribution within cancer tissues following intratumoral administration is a critical issue for magnetic hyperthermia because it leads to the under-heating of regions within tumors.[61,62]

Microscopic analyses of Prussian blue-stained sections of various organs, including endometriosis grafts, collected at 24 hours and 5 days post-administration revealed that the spleen and liver sequester a significant amount of KDR-MN after intravenous injection and eliminate them from the body (Figure S6–S8). Quantification of iron oxide-based nanoparticles in various tissues was performed by measuring Prussian blue-stained areas with ImageJ software as previously described.[63,64] The percentage of Prussian blue-stained

tissue area is provided (Figure S8). The analysis demonstrates that nanoparticles accumulate significantly in the spleen (1.1%), endometriosis grafts (0.7%), liver (0.4%), and, to a lesser extent, in other organs (< 0.1%) 24 hours after administration (Figure S8a). Prussian blue signal was also detected in the spleen (1.3%) and endometriosis lesions (1.2%) 5 days after injection. In contrast, it was negligible in other organs, including the liver, indicating that nanoparticles had been cleared from these tissues (Figure S8b). Therefore, we chose to perform nanoparticle-mediated magnetic hyperthermia 5 days after KDR-MN administration.

In the next step, we evaluated the ability of the systemically injected KDR-MN to generate heat in endometriotic grafts under AMF. Intralesional temperature profiles were directly recorded with a fiber optic probe. Our results reveal that 5 days after IV injection (3 mg Fe per kg), the KDR-MN elevated the temperature inside of grafts up to 51.6 ± 1.2 °C, reaching 46 °C within 15.5 minutes (Figure 5c, red curve). In contrast, non-targeted MN raised the temperature only to 49.3 ± 1.8 °C, reaching 46 °C within 19.5 minutes under the same experimental conditions (Figure 5c, black curve). The ability of non-targeted and KDR-targeted nanoparticles to increase the temperature in grafts above 46 °C suggests that both nanoparticles accumulate efficiently in endometriotic tissue via passive targeting. The observed difference in heating rates during AMF exposure could be associated with increased retention of passively accumulated KDR-MN in endometriosis grafts compared to non-targeted MN within 5 days after administration. This is consistent with prior work showing that targeting ligands improve the internalization of passively delivered nanoparticles by cells expressing target receptors, resulting in their enhanced retention at disease sites (e.g., cancer or endometriosis).[21,65] Of note, our results validate the KDR peptide significantly increases MN uptake into the endometriotic stromal cells (Figure 4a and Figure S3).

The obtained data highlight the superior in vivo heating efficiency of the developed MN compared to previously reported magnetic nanoparticles. To our knowledge, aside from our previous report,[20] there are no published studies demonstrating nanoparticles capable of increasing temperatures in either cancer or endometriotic lesions above 43 °C after systemic injection at a clinical dose (< 10 mg kg^{-1}). We reported the heating efficiency of non-spherical iron oxide nanoparticles containing manganese and cobalt to be 4.7 times lower (SAR = 1715 W g^{-1}) than that of MN (SAR = 8057 W g^{-1}), described herein, under identical experimental conditions. Our previously reported nanoparticles were capable of increasing intratumoral temperature only up to 44 °C after IV administration at a higher dose (6 mg kg^{-1} Fe) and the achieved intratumoral temperature only inhibited tumor growth.[20] In current studies, we also demonstrate that these previously reported nanoparticles (6 mg kg^{-1} Fe) elevate the temperature inside of endometriotic grafts up to 43 °C (Figure S9). In contrast, the new MN (3 mg kg^{-1} Fe) raised the intralesional temperature above 50 °C. Of note, temperatures above 46 °C can completely eradicate cancer or endometriosis tissues. [13,22]

Importantly, our current results demonstrate that the increase in temperature of tissue immediately surrounding endometriotic grafts was negligible (Figure 5d, black curve) and was similar to the temperature increase in a graft exposed to AMF alone (no KDR-MN,

(Figure 5d, gray curve). This suggests that systemically injected KDR-MN efficiently localizes in endometriotic grafts, but not in tissue adjacent to the grafts (Figure 5d inset and Figure S8), and heat transfer from the graft to the adjacent tissue is negligible. Moreover, our results validate that the employed AMF is safe because it significantly heats only tissues containing nanoparticles (Figure 5c and Figure 5d).

The main requirement for AMF during magnetic hyperthermia is to diminish non-selective heating of healthy tissue.[66,67] Hergt et al. proposed that AMF with the product of frequency (f) and field strength (H) of $> 5 \times 10^9$ A m^{-1} s^{-1} could potentially cause excessive non-selective heating of healthy and cancer tissues due to the generation of eddy currents.[68] Although our AMF parameters ($f = 420$ kHz; $H = 26.9$ kA m^{-1}, $H \times f = 11.2 \times 10^9$ A m^{-1} s^{-1}) are not exactly in the range suggested by Hergt et al., current results (Figure 5d) and our previous reports validate that employed AMF (420 kHz; 26.9 kA m^{-1}) alone does not increase temperatures in endometriosis lesions, cancer tumors and rectum by more than 2.5 °C.[19,20] Clinical studies revealed that median rectal temperature of patients with prostate cancer recorded during magnetic hyperthermia therapy reached 39.8 °C (normal rectal temperature: 37.5 °C) and the applied AMF was well tolerated with no notable adverse effects.[69] Our current and previously published results also confirm that the applied AMF (420 kHz; 26.9 kA m^{-1}) does not cause any side effects in animals (Figure 9).[19,20] Therefore, clinical safety studies will be required for each planned magnetic hyperthermia regimen performed with a particular AMF system. We also demonstrate that our developed nanoparticles exhibit a high heating efficiency upon exposure to AMF with field strengths lower than 26.9 kA m^{-1} (Figure S10). For example, when exposed to a 420 kHz AMF with a field strength of 26.9 kA m^{-1}, which was used in animal studies, and 11.9 kA m^{-1}, which satisfies the Hergt criterion ($H \times f = 5 \times 10^9$ A m^{-1} s^{-1}), the temperature in the nanoparticle solution reached 66.7 °C and 64.8 °C, respectively.

Our results also revealed that developed nanoparticles demonstrate high heating efficiency upon exposure to AMF with field strengths 18 kA m^{-1} (Figure S10). The AMF applicator MFH 300F® (subsequently renamed as Nanoactivator® F100) used in clinical trials operates at field strengths ranging from 0 to 18 kAm^{-1} and a fixed frequency of 100 kHz.[70] Our current magnetic hyperthermia system generates AMF with a fixed frequency of 420 kHz and variable field strengths. Therefore, the therapeutic efficacy of KDR-MN-mediated magnetic hyperthermia using clinically tested AMF parameters (100 kHz, 18 kA/m) must be evaluated in future studies.

Finally, we validated that the endometriotic tissues in mice, intravenously injected with KDR-MN (3 mg Fe per kg), can be eradicated after 20 minutes of exposure to AMF at day 5 post-administration, with no recurrence (Figure 5e, red curve). In contrast, the growth of grafts was not affected by KDR-MN (Figure 5e, blue curve) or AMF exposure alone (gray curve). The observed variability in graft size at the onset of treatment, as well as their subsequent growth rates, is related to hormone pre-treatment (Figure 5e). In our studies, small pieces of macaque tissue are surgically implanted in subcutaneous pockets of mice. To reduce the impact of grafting surgery on the study outcome, exogenous estradiol (E2) and progesterone (P) are sequentially administered to the mice to recapitulate a primate ovarian cycle. During this cycle, P withdrawal triggers tissue breakdown and bleeding similar to

menstruation, and the grafts regrow under the effect of E2. Thus, unlike cancer grafts which grow continuously over time, the cyclic administration of hormones creates individual (variously sized) endometriotic lesions with different growth rates similar to the disease in women. Our results show that magnetic hyperthermia mediated by KDR-MN can eradicate lesions of various sizes (Figure 5f).

2.6.   MRI properties of magnetic nanoparticles

To assess the potential medical imaging properties of the KDR-MN, in vitro and in vivo assessment of MRI signal changes were tested. In vitro, these magnetic nanoparticles showed significant T2-weighted signal loss compared to a control dextrose solution (5% dextrose, 0 μg mL^{-1}) at increasing echo times (Figure 6a, b).

Moreover, when evaluating R2 relaxation rates, there was a concentration-dependent increase in R2 that was substantially larger for the KDR-MN nanoparticle compared to a commercially available iron-oxide agent, ferumoxytol (Figure 6a, c).[71] On average, the R2 relaxation rate was 82.4% higher than that of ferumoxytol for a given concentration. Ferumoxytol is a magnetic iron oxide nanoparticle coated with polyglucose sorbitol carboxymethyl ether (diameter: 17 – 31 nm).[30] These FDA-approved nanoparticles for iron deficiency are being rapidly explored as MRI agents due to their ability to enhance signal contrast in the local microenvironment relative to background tissues.[72] This enhancement is seen primarily as signal loss in the tissue microenvironment on T2-weighted MRI secondary to shortening T2 (and increasing R2) relaxation times in adjacent protons. The more robust signal dropout and increased R2 relaxation seen in the KDR-MN may be secondary to the additional accelerated R2 relaxation effects from cobalt, although, potentially, the geometric shape of the nanoparticles may also be contributory.[73]

The observed T2-weighted signal changes enabled localization of our magnetic nanoparticles in vivo by MRI as a molecular imaging agent. In vivo injection of KDR-MN detected endometriosis grafts in a mouse model. Figure 7 demonstrates representative T2-weighted MR images of endometriotic grafts in mice IV injected with saline and KDR-MN, respectively. A dashed circle depicts the endometriosis graft in each mouse.

When normalized to signal intensity of the adjacent background skeletal muscle, the acquired images demonstrated nearly 50% visual T2 signal dropout and negative contrast properties of KDR-MN in endometriotic grafts relative to the uninjected control at a concentration (3 mg Fe per kg) relevant for therapeutic hyperthermia (Figure 7i).

Endometriosis lesions spread widely throughout the pelvic and lower abdominal regions and, in some cases, can be found at distal locations (e.g., liver, lungs, and brain).[74] Because MRI can be used before magnetic hyperthermia to detect the location of endometriotic lesions containing KDR-MN, AMF can be applied to small local areas where lesions are located without exposing a whole region of the body or the entire body. As proof of concept, the rear third of a mouse containing one endometriosis graft was placed inside the round induction coil and exposed to the AMF for 20 minutes while another graft was outside of the coil. Our results show that by exposing a specific area of the body, it is possible to eradicate targeted endometriotic grafts without affecting nearby grafts containing KDR-MN (7 mm

distance) in the same mouse (Figure 8). As a result, the potential heating of normal tissues containing nanoparticles can be avoided.

This project aimed to develop nanoparticles for systemic delivery to endometriotic lesions that can be heated by currently available and future optimized magnetic hyperthermia systems. For instance, Magnetic Insight released the HYPER system capable of specific AMF delivery to targeted tissue with millimeter accuracy.[75,76] The same system can also be employed for real-time, highly sensitive detection of disease tissues containing magnetic nanoparticles using magnetic particle imaging (MPI), a new non-invasive 3D imaging technique with high spatial and temporal resolution.[76,77] Finally, MPI allows the quantification of low concentrations of magnetic nanoparticles in tissues and heating dose calculations.[76] Liu et al. also revealed that the physical mechanism behind the HYPER system could be employed to trigger drug release from thermally responsive liposomes, allowing for millimeter-scale drug delivery localization.[78]

2.7. Toxicity studies

Importantly, our results reveal that the KDR-MN-based magnetic hyperthermia is a safe therapy without noticeable adverse effects. None of the treated mice lost over 10% of their body weight (Figure 9a), died or demonstrated any toxicity symptoms during a 42-day study. The biochemical markers for the kidney function (creatinine (Cr) and blood urea nitrogen (BUN)), liver function (alanine aminotransferase (ALT), and alkaline phosphatase (ALP)), muscle and heart function (creatine kinase), as well as protein and electrolyte serum levels, were measured 42 days after the treatment (Figure 9b, c, d). All treated mice demonstrated normal serum biochemical values in comparison to control animals.

We realize that there might be concerns of putative cobalt leaching from the prepared KDR-MN resulting in high blood cobalt levels and toxicity. For example, cobalt-containing alloys are commonly used in hip prostheses, and high cobalt amounts can be released into the systemic circulation for an extended period due to implant wear, causing clinical changes.[79] In addition, cobalt dietary supplements are also available in the USA to improve red blood cell production, protein synthesis, and fat and carbohydrate metabolism, thereby raising blood cobalt levels following oral administration.[80] However, there is currently no consensus in the literature regarding the exact blood cobalt concentrations that cause adverse effects in patients.[79] According to the available reports, adverse responses of any type are unlikely to occur in humans below blood cobalt concentrations of 300 µg L^{-1}.[79] For example, in a three-month clinical trial with people who voluntarily took a cobalt supplement (daily cobalt dose: 0.080–0.19 mg kg^{-1}), cobalt blood concentrations ranging from 9.4 to 117 µg L^{-1} were not associated with any clinically significant changes.[81] Blood cobalt concentrations of 700–800 µg L^{-1} and above, according to Finley et al., may be linked to an increased risk of adverse effects.[80] Notably, patients who take cobalt dietary supplements for many months and those with failed hip implants have chronically elevated cobalt blood levels.[81,82] Our magnetic hyperthermia therapy, however, requires a single injection of cobalt-doped nanoparticles at a cobalt dose of 0.11 mg per kg of body weight (3 mg kg^{-1} Fe). In a separate study, we found that 24 and 96 hours after injection with our nanoparticles (0.11 mg kg^{-1} Co), cobalt blood concentrations in mice were 52

and 43 μg L^{-1}, respectively, which is significantly lower than 300 μg L^{-1}.[79,81] It must also be emphasized that the cobalt toxicity discussed above and the reported cobalt blood concentrations are related to the blood levels of free cobalt ions.[83] In our studies, however, injected cobalt is incorporated into iron oxide nanoparticles. As a result, the measured cobalt blood levels are most likely a combination of cobalt incorporated into nanoparticles and free cobalt ions released as nanoparticles degrade in organs of the reticuloendothelial system (the spleen and liver). Therefore, actual blood levels of free cobalt ions are likely to be lower than measured.

Clearly, before these nanoparticles are translated into clinical trials, their pharmacokinetic and safety profiles must be thoroughly evaluated in a variety of animal models. However, our current toxicity studies in mice are promising because none of the treated animals demonstrated any toxicity symptoms during a 42-day study (Figure 9). Our findings are consistent with previous reports demonstrating that cobalt ferrite nanoparticles injected at comparable or higher cobalt doses do not cause obvious toxicity in animals.[84,85] For example, Shakil et al. reported that a single intravenous injection of cobalt ferrite nanoparticles at a dose of 20 mg kg^{-1} (cobalt mass fraction = 18.36% or ~3.6 mg kg^{-1} Co) has no effect on rats' physical, biochemical, hematological, or histopathological parameters.[85]

3. Conclusion

This study developed a novel non-surgical therapy named systemically delivered magnetic hyperthermia for safe and efficient ablation of endometriotic lesions. To realize the full potential of this treatment modality, we engineered novel endometriosis-targeted magnetic nanoparticles capable of (i) efficient accumulation in endometriotic lesions after a single IV administration (3 mg Fe per kg) and (ii) generation of therapeutic temperatures (> 50 °C) in these lesions upon exposure to safe AMF. In vivo studies in mice bearing macaque endometriosis grafts validate that the developed nanoparticle completely ablate endometriotic grafts without adverse effects after a single 20-minute exposure to AMF. Furthermore, these nanoparticles were shown to have the potential to be employed as an MRI contrast agent to aid in the diagnosis of endometriotic lesions before AMF exposure. The obtained results suggest that nanoparticle-mediated magnetic hyperthermia can potentially provide an efficient non-surgical approach to eradicate endometriotic lesions and shift the paradigm for endometriosis treatment. Validation of the developed systemically delivered magnetic hyperthermia in large animal models is important for advancing this therapy to women. Our future steps will be to verify whether the safety and efficacy of the developed treatment modality can be translated to old-world nonhuman primates that spontaneously develop endometriosis and are functionally similar to women.

4. Experimental Section/Methods

Materials:

n-Octyl ether was obtained from Tokyo chemical industry Co. (Tokyo, Japan). Oleic acid and cobalt (II) chloride hexahydrate (CoCl$_2$·6H$_2$O) were purchased from Alfa Aesar (Ward Hill, MA, USA). SiNc (silicon 2,3-naphthalocyanine bis (trihexylsilyloxide)) was purchased

from Alfa Chemistry (Ronkonkoma, NY, USA). Iron (III) acetylacetonate (($Fe(acac)_3$) and oleylamine were obtained from ACROS Organics (Fair Lawn, NJ, USA) and Sigma-Aldrich (St. Louis, MO, USA), respectively. PEG–PCL (methoxy poly(ethylene glycol)-b-poly(ε-caprolactone), MW: PEG(5k)-PCL(10k)) and Carboxyl PEG-PCL (MW: HOOC-PEG(5k)-PCL(10k))) were purchased from Advanced Polymer Materials Inc. (Montreal, Canada). KDR peptide (ATWLPPR) was purchased from Biomatik (Wilmington, DE, USA). N,N′-dicyclohexylcarbodiimide (DCC) was purchased from Oakwood Products, Inc (West Columbia, SC, USA). N,N'-hydroxysuccinimide (NHS) was purchased from Sigma Aldrich (St. Louis, MO, USA). A quantitative fluorometric peptide assay was obtained from Pierce (Waltham, MA, USA). Spherical iron oxide nanoparticles dispersed in chloroform were purchased from Ocean NanoTech (San Diego, CA, USA).

Synthesis of cobalt-doped hexagonal nanoparticles:

A modified thermal decomposition method was used to prepare cobalt-doped iron oxide nanoparticles with a hexagonal shape.[20,86–88] Briefly, $CoCl_2$ $6H_2O$ (1.5 mmol) and $Fe(acac)_3$ (5.0 mmol) were introduced to a mixture of n-octyl ether (30.0 mL), oleylamine (2.2 mL) and oleic acid (2.5 mL) in a three-neck round-bottom flask and heated to 300 °C at a ramping rate of 840 °C h^{-1} under nitrogen flow and 300 revolutions per minute (rpm) stirring. The reaction mixture was cooled to ambient temperature after 90 minutes and the reaction product was precipitated by adding ethanol (30 mL), followed by centrifugation at 7830 rpm for 10 minutes. The product was re-dispersed in hexane (10 mL, 8 mg mL^{-1}) and added to a three-neck round-bottom flask containing the same precursors (e.g., $CoCl_2$ $6H_2O$, $Fe(acac)_3$, oleic acid, etc.) used in the initial reaction. Under controlled nitrogen flow and vigorous stirring, the reaction mixture was heated to 300 °C at a rate of 840 °C h^{-1}. After 90 minutes, it was cooled to ambient temperature and precipitated with ethanol as described above. The obtained precipitate was washed twice with a 1:4 tetrahydrofuran (THF): ethanol (25 mL) to obtain the final nanoparticles dispersed in THF.

Characterization of hexagonal and spherical nanoparticles:

The size and morphology of the synthesized nanoparticles were evaluated using FEI Tecnai™ Spirit Transition Electron Microscope equipped with an Eagle™ 2K CCD multiscan camera (FEI, Hillsboro, OR, USA).[89] Chemical composition of the nanoparticles was analyzed by energy-dispersive X-ray spectroscopy (EDX) using an FEI 80–300 kV Titan Analytical Transmission Electron Microscope (FEI, Hillsboro, OR, USA). The heating efficiency of hexagonal and spherical nanoparticles under AMF was measured and compared in terms of specific absorption rate (SAR) by using the equation below in accordance with the previously published procedure.[19,20]

$$SAR = (CVs/m) \times (dT/dt),$$

where C is the specific heat capacity of the medium, Vs is the sample volume, m is the mass of magnetic nanoparticle suspended in the medium, and dT/dt is the initial slope of the time-dependent temperature curve.

Vials containing tested nanoparticles in THF (1 mg mL^{-1} Fe) were thermally insulated and placed in a water-cooled 6-turn copper coil (4 cm inner diameter). Each vial was then subjected to AMF (420 kHz, 26.9 kA m^{-1}) produced by an induction heating system (MSI Automation, Wichita, KS, USA) and the temperature was recorded with a probe (Neoptix Inc., QC, Canada) as previously reported.[20,90] The obtained data were used to generate time-dependent temperature curves.

Conjugation of KDR targeting peptide to PEG-PCL polymer:

DCC (2 equivalent to Carboxyl PEG-PCL) and NHS (4 equivalent to Carboxyl PEG-PCL) were added to a solution of Carboxyl PEG-PCL (32 mg, 2.1 μmol) in Acetonitrile (1.5 mL). After 1 hour of mixing, KDR peptide (2 mg, 2.4 μmol) was added to the reaction mixture and stirred overnight at ambient temperature. The conjugation was confirmed using quantitative fluorometric peptide assay according to the manufacturer's protocol. The fluorescence of the product mixed with the amine-reactive fluorescent detection reagent was measured at 475 nm. The amine-reactive reagent specifically labeled the N-terminus of unconjugated peptides. The conjugation yield was 89.2%.

Synthesis and characterization of non-targeted and KDR-targeted magnetic nanoparticles:

Non-targeted and KDR-targeted MN were prepared using the modified solvent evaporation method.[38] To prepare non-targeted MN, PEG-PCL (50 mg mL^{-1}) and synthesized MN (1 mg mL^{-1}) were mixed in THF (1 mL). Then, dextrose 5% in water (1 mL) was added to the prepared THF mixture and stirred for 3 min. The resulting solution was left overnight at ambient temperature to evaporate THF. To prepare KDR-modified MN, a mixture of the synthesized KDR-PEG-PCL (5 mg mL^{-1}) and PEG-PCL (45 mg mL^{-1}) was used in the first step of the above-described procedure. Finally, non-targeted and KDR-targeted nanoparticles loaded with a fluorescence dye (Nile Red or SiNc) were prepared by introducing either Nile Red (0.2 mg mL^{-1}) or SiNc (0.2 mg mL^{-1}) to the THF mixture as described above.

Cryogenic transmission electron (cryo-TEM) microscope, Glacios™ Cryo-TEM with Gatan K3 Camera (Thermo Fisher Scientific, Waltham, MA), was employed to assess the morphology of the prepared non-targeted and KDR-MN as previously reported.[91] Their hydrodynamic size, PDI and zeta potential were determined by ZetaSizer NanoSeries (Malvern, Worcestershire, UK) as previously described.[90] To confirm encapsulation of a corresponding dye, fluorescence spectra of both non-targeted and KDR-modified nanoparticles were recorded and analyzed using a Cary Eclipse R3896 fluorescence Varian spectrophotometer (Mulgrave, Victoria, Australia). Finally, the heating efficiency of KDR-MN under AMF was measured as described above.

Primary Tissue Culture:

Endometriosis, endometrium and kidney tissues were collected from rhesus macaques at necropsy. Random samples of the endometrium and endometriosis lesions were frozen, cryosectioned, and the expression of KDR by these tissues was tested by immunohistochemistry (AB # PA5–16487; Thermo Fisher Scientific, Waltham, MA). Macaque primary cells were isolated from the collected tissues according to our previously published protocol.[22] These cells were propagated in DMEM with 10% FBS, antimycotic

and antibiotic and allocated to treatments. The KDR expression in the collected tissues and isolated cells was evaluated by qPCR.

Cellular Internalization of non-targeted and KDR-targeted nanoparticles:

Primary macaque endometriosis, endometrium, and kidney cells were seeded in 6-well plates (30,000 cells per well) and incubated with non-targeted and KDR-targeted nanoparticles loaded with Nile Red (0.5 μg mL^{-1}) for 24 hours. Afterward, the medium was removed, cells were washed with DPBS three times and collected. Cell fluorescence generated by internalized Nile Red was measured using a BD Accuri C6 flow cytometer (BD Biosciences, CA, USA). In addition, Zeiss LSM880 laser scanning confocal microscope (Zeiss, Oberkochen, Germany) was used to obtain fluorescence images of endometriosis cells incubated for 24 hours with non-targeted and KDR-targeted nanoparticles loaded with Nile Red.

In Vitro Magnetic Hyperthermia generated by non-targeted and KDR targeted magnetic nanoparticles:

Monolayers of primary macaque endometriosis cells seeded in 100 mm dishes (200,000 cells per well) were incubated with non-targeted MN and KDR-MN (25 μg mL^{-1} Fe) for 24 hours, respectively. Collected cells were transferred to microcentrifuge tubes, centrifuged at 10,000 rpm for 1 minute to form cell pellets, and then exposed to AMF (420 kHz, 26.9 kA m^{-1}) for 30 minutes as described above. Cells subjected to AMF (no nanoparticles) and cells incubated with nanoparticles (no AMF) were used as controls. Then, treated cells were seeded in 96-well plates (10,000 cells per well), cultured for 48 hours, and their viability was assessed with a Calcein AM assay.[90]

In vivo studies:

All animal studies were approved by the Institutional Animal Care and Use Committees at Oregon Health and Science University and Oregon State University (approval number: IP00000033).

A mouse model for endometriosis:

The macaque endometrium tissues were obtained from monkeys in the mid secretory phase of the menstrual cycle and transplanted into subcutaneous pockets of 3-week old female ICR SCID mice (Taconic Biosciences, Germantown, NY, USA) according to our previously reported procedure (up to 5 grafts per mouse).[22] The mice were treated sequentially with estradiol (E2; 90-day release plus progesterone (P4; 14-day release) delivered by implants (Innovative Research of America, Sarasota, FL, USA). The implants produce primate levels of E2 (100–120 pg mL^{-1}) and P4 (10–15 ng mL^{-1}) in the mice. P4 implants were replaced after 28 days to create human-length artificial menstrual cycles in the mice. Under these conditions, the grafts develop into lesions that grow in response to E2 and bleed in response to P4 withdrawal, similar to endometriosis in women and monkeys.

Evaluation of KDR-MN biodistribution:

Six mice with multiple endometriotic xenografts were IV injected with 200 μL of KDR-MN (3mg Fe per kg) loaded with a NIR dye (SiNc). The Pearl Impulse Small Animal Imaging System (LI-COR, Lincoln, NE, USA) was used to record the NIR fluorescence signal generated by SiNc in the mouse body at 24 hours and 5 days post-injection (three mice per time point).[92] Endometriotic grafts and various organs were collected 24 hours and 5 days post-euthanasia, sectioned and stained with Prussian blue using the iron stain kit (Polysciences, Inc., Warrington, PA, USA) according to our previously published protocol.[20] The stained tissues were imaged with a Keyence BZ-X Fluorescence Microscope (Keyence, Osaka, Japan).

Evaluation of nanoparticles heating efficiency:

Mice with multiple lesions were IV injected with non-targeted MN (3mg Fe per kg), KDR-targeted MN (3mg Fe per kg) or saline and subjected to the AMF at 5 days after nanoparticles administration (three mice per group). Before AMF exposure, mice were anesthetized with isoflurane and Neoptix T1 temperature probes were placed into the core of the endometriotic graft or adjacent to the graft. Each animal was placed inside the round induction coil (6 turns, 4 cm inner diameter), and temperature changes were recorded during AMF exposure.[20,22]

Assessment of the therapeutic efficacy of magnetic hyperthermia:

To assess the ability of magnetic hyperthermia to ablate endometriotic lesions, five mice were injected IV with a single dose of KDR-MN (3 mg Fe per kg), placed inside the round induction coil on day 5 post-injection and subjected to AMF (420 kHz, 26.9 kA m^{-1}) for 20 minutes. The effect of AMF alone on endometriotic lesions was tested by exposing four saline-injected mice to AMF (420 kHz, 26.9 kA m^{-1}) as described above. Four mice injected IV with a single dose of KDR-MN (3 mg Fe per kg) were used to evaluate the effect of nanoparticles on the growth of endometriotic lesions. In the control group, four mice were injected with saline. The growth of grafts was measured by caliper for four weeks after treatment. The following equation was employed to calculate graft volumes:

$$V = W^2 \times L/2,$$

where V, W, and L are volume, width, and length of grafts, respectively.

At the end of the study, blood samples were collected and analyzed by the IDEXX laboratory (Portland, OR, USA).

Evaluation of cobalt blood levels in mice:

Six mice without endometriosis grafts were IV injected with KDR-MN (3mg Fe per kg), blood samples were collected by cardiac puncture at 24 and 96 hours post-administration and cobalt concentrations were measured using Inductively Coupled Plasma Mass Spectrometry (ICP-MS) at the Oregon Health & Science University (OHSU) Elemental Analysis Core as previously described.[20]

MRI studies:

KDR-MN and ferumoxytol ($1mg\ mL^{-1}$) were used as starting materials for the comparative in vitro dilution series. These were diluted with 5% dextrose solution to achieve target concentrations between 2 and 10 $\mu g\ mL^{-1}$. This range of concentrations was chosen to be within the expected concentrations for therapeutic treatment in vivo. The control concentration of 0 $\mu g\ mL^{-1}$ was comprised of a 5% dextrose solution. A total volume of 2 mL of each target concentration was created and placed in individual 1.5 mL microcentrifuge tubes. For MRI, a 50 mL centrifuge tube was modified with holes along its side to fit the 1.5 mL microcentrifuge tubes as a holder and then filled with water to create a uniform background. Two tubes at a time were imaged.

Magnetic resonance imaging was performed on a Bruker BioSpin GmbH 11.75 Tesla (T)/500MHz horizontal magnet equipped with ParaVision version 5.1 software (Ettlingen, Germany). The following imaging parameters were used: T2 – weighted RARE acquisition with a repetition time (TR) of 2000 milliseconds (ms), 192×192 matrix size, slice thickness of 1 mm, with flip angle set to 180 degrees and a 3.2 cm $\times$ 3.2 cm display field of view (DFOV). Varying echo times (TE) of 9, 18, 27, and 36 ms were employed. T2 relaxation times were fit using a 2-parameter nonlinear least squares fit in Matlab (Mathworks, MA, USA) using the signal across the four echoes in each pixel. R2 values were calculated by taking the reciprocal of the fitted T2 values. The mean R2 values were calculated in a 15×15 pixel region in the center of each phantom.

Mice (two animals per group) bearing multiple subcutaneous endometriotic grafts were IV injected with 200 μL of KDR-MN (3mg Fe per kg) or saline (control). Graft imaging by MRI was performed 24 hours after injection and immediately after euthanization. The following imaging parameters were used: Gradient Images: T2*-weighted fast low angle shot (FLASH) gradient-echo sequence with a TR of 500 ms, a matrix size of 128×192 slice thickness of 1 mm, 30 slices, with flip angle set to 40 degrees. TE of 1.12, 3.0, 4.5, and 6.0 ms were employed. The display field of view was 3.3×3.8cm. T2 Images: T2 weighted rapid acquisition with relaxation enhancement (RARE) sequence with a TR 7000–8150 ms, TE of 23.65 ms, echo train length (ETL) of 8, a matrix size of 512×256, slice thickness of 0.5 mm, 60 slices and flip angle set to 180 degrees, and DFOV = 3.5×3.5cm. MR images of eight grafts were recorded. The MRI signal in the graft and muscle were analyzed using ImageJ (National Institutes of Health (NIH), MD, USA) as previously described.[93] The mean gray value, which is the sum of the gray value of the region of interest (ROI) divided by the number of pixels in the ROI, was used to represent signal intensity. The mean signal ratio is calculated by dividing the graft signal by the muscle signal in the same image, thereby reducing effects from coil sensitivity and signal-to-noise variations.

Statistical Analysis:

In these studies, no data pre-processing was performed. Data were presented as mean values ± standard deviation (mean ± SD) from three to twenty separate measurements. The sample size for each statistical analysis (n) is indicated in the figure legends. The two-tailed unpaired t-test was used for statistical comparisons between two groups. One-way analysis of variance (ANOVA) was used to test statistical significance for more than two groups.

Statistical methods used to assess significant differences between groups in each study are specified in the figure legends. Differences between groups were considered statistically significant at $p < 0.05$. Statistical significance is denoted as $*p < 0.05$, $**p < 0.01$, $***p < 0.001$ and $****p < 0.0001$. GraphPad Prism v9 (GraphPad Software, CA, USA) was used for statistical analyses.

Supplementary Material

Refer to Web version on PubMed Central for supplementary material.

Acknowledgments

References

[1]. As-Sanie S, Black R, Giudice LC, Gray Valbrun T, Gupta J, Jones B, Laufer MR, Milspaw AT, Missmer SA, Norman A, Taylor RN, Wallace K, Williams Z, Yong PJ, Nebel RA, Am. J. Obstet. Gynecol 2019, 221, 86. [PubMed: 30790565]

[2]. Koninckx PR, Ussia A, Adamyan L, Wattiez A, Donnez J, Fertil. Steril 2012, 98, 564. [PubMed: 22938769]

[3]. Taylor HS, Kotlyar AM, Flores VA, Lancet 2021, 397, 839. [PubMed: 33640070]

[4]. Alimi Y, Iwanaga J, Loukas M, Tubbs RS, Cureus 2018, 10, e3361. [PubMed: 30510871]

[5]. Parazzini F, Hum. Reprod 1999, 14, 1332. [PubMed: 10325288]

[6]. Marcoux S, Maheux R, Berube S, Engl N. J. Med 1997, 337, 217.

[7]. Guo SW, Hum. Reprod. Update 2009, 15, 441. [PubMed: 19279046]

[8]. Hilger I, Int. J. Hyperthermia 2013, 29, 828. [PubMed: 24219800]

[9]. Luo S, Wang LF, Ding WJ, Zhou MJ, Jin HK, Su SF, Ouyang WW, OA Cancer 2014, 2, 2.

[10]. Johannsen M, Gneveckow U, Eckelt L, Feussner A, Waldofner N, Scholz R, Deger S, Wust P, Loening SA, Jordan A, Int. J. Hyperthermia 2005, 21, 637. [PubMed: 16304715]

[11]. Maier-Hauff K, Rothe R, Scholz R, Gneveckow U, Wust P, Thiesen B, Feussner A, von Deimling A, Waldoefner N, Felix R, Jordan A, J. Neurooncol 2007, 81, 53. [PubMed: 16773216]

[12]. Wust P, Gneveckow U, Johannsen M, Bohmer D, Henkel T, Kahmann F, Sehouli J, Felix R, Ricke J, Jordan A, Int. J. Hyperthermia 2006, 22, 673. [PubMed: 17390997]

[13]. Jang JT, Lee J, Seon J, Ju E, Kim M, Kim YI, Kim MG, Takemura Y, Arbab AS, Kang KW, Park KH, Paek SH, Bae S, Adv. Mater 2018, 30, 1704362.

[14]. Moy AJ, Tunnell JW, Adv. Drug Deliv. Rev 2017, 114, 175. [PubMed: 28625829]

[15]. Shetake NG, Balla MMS, Kumar A, Pandey BN, Radiat J. Cancer Res. 2016, 7, 13.

[16]. Torres-Lugo M, Rinaldi C, Nanomedicine (Lond) 2013, 8, 1689. [PubMed: 24074390]

[17]. Deatsch AE, Evans BA, J. Magn. Magn. Mater 2014, 354, 163.

[18]. Kumar CS, Mohammad F, Adv. Drug Deliv. Rev 2011, 63, 789. [PubMed: 21447363]

[19]. Albarqi HA, Demessie AA, Sabei FY, Moses AS, Hansen MN, Dhagat P, Taratula OR, Taratula O, Pharmaceutics 2020, 12, 1020.

[20]. Albarqi HA, Wong LH, Schumann C, Sabei FY, Korzun T, Li X, Hansen MN, Dhagat P, Moses AS, Taratula O, Taratula O, ACS Nano 2019, 13, 6383. [PubMed: 31082199]

[21]. Moses AS, Demessie AA, Taratula O, Korzun T, Slayden OD, Taratula O, Small 2021, 17, e2004975. [PubMed: 33491876]

[22]. Moses AS, Taratula OR, Lee H, Luo F, Grenz T, Korzun T, Lorenz AS, Sabei FY, Bracha S, Alani AWG, Slayden OD, Taratula O, Small 2020, 16, e1906936. [PubMed: 32250034]

[23]. Guo X, Li W, Zhou J, Hou W, Wen X, Zhang H, Kong F, Luo L, Li Q, Du Y, You J, Small 2017, 13, 1603270.

[24]. Gibbs SL, Quant. Imaging Med. Surg 2012, 2, 177. [PubMed: 23256079]

[25]. Hoopes PJ, Moodie KL, Petryk AA, Petryk JD, Sechrist S, Gladstone DJ, Steinmetz NF, Veliz FA, Bursey AA, Wagner RJ, Rajan A, Dugat D, Crary-Burney M, Fiering SN, Proc. SPIE Int. Soc. Opt. Eng 2017, 10066.

[26]. Hoopes PJ, Wagner RJ, Duval K, Kang K, Gladstone DJ, Moodie KL, Crary-Burney M, Ariaspulido H, Veliz FA, Steinmetz NF, Fiering SN, Mol. Pharm 2018, 15, 3717. [PubMed: 29613803]

[27]. Hayashi K, Nakamura M, Sakamoto W, Yogo T, Miki H, Ozaki S, Abe M, Matsumoto T, Ishimura K, Theranostics 2013, 3, 366. [PubMed: 23781284]

[28]. Nguyen KL, Yoshida T, Han F, Ayad I, Reemtsen BL, Salusky IB, Satou GM, Hu P, Finn JP, J. Magn. Reson. Imaging 2017, 45, 804. [PubMed: 27480885]

[29]. Pham HN, Pham TH, Nguyen DT, Phan QT, Le TTH, Ha PT, Do HM, H. T. M. N, X. P. Nguyen, Adv. Nat. Sci.: Nanosci. Nanotechnol 2017, 8 025013.

[30]. Access data.fda.gov. Ref. ID: 4216092. https://www.accessdata.fda.gov/drugsatfda_docs/label/2018/022180s009lbl.pdf

[31]. Xie J, Yan C, Yan Y, Chen L, Song L, Zang F, An Y, Teng G, Gu N, Zhang Y, Nanoscale 2016, 8, 16902. [PubMed: 27427416]

[32]. Xie J, Zhang Y, Yan C, Song L, Wen S, Zang F, Chen G, Ding Q, Yan C, Gu N, Biomaterials 2014, 35, 9126. [PubMed: 25106772]

[33]. Cho M, Cervadoro A, Ramirez MR, Stigliano C, Brazdeikis A, Colvin VL, Civera P, Key J, Decuzzi P, Nanomaterials (Basel) 2017, 7, 72.

[34]. Guardia P, Di Corato R, Lartigue L, Wilhelm C, Espinosa A, Garcia-Hernandez M, Gazeau F, Manna L, Pellegrino T, ACS Nano 2012, 6, 3080. [PubMed: 22494015]

[35]. He S, Zhang H, Liu Y, Sun F, Yu X, Li X, Zhang L, Wang L, Mao K, Wang G, Lin Y, Han Z, Sabirianov R, Zeng H, Small 2018, 14, e1800135.

[36]. Noh SH, Na W, Jang JT, Lee JH, Lee EJ, Moon SH, Lim Y, Shin JS, Cheon J, Nano Lett. 2012, 12, 3716. [PubMed: 22720795]

[37]. Wang H, Shrestha TB, Basel MT, Pyle M, Toledo Y, Konecny A, Thapa P, Ikenberry M, Hohn KL, Chikan V, Troyer DL, Bossmann SH, J. Mater. Chem. B 2015, 3, 4647. [PubMed: 32262479]

[38]. Taratula O, Doddapaneni BS, Schumann C, Li X, Bracha S, Milovancev M, Alani AWG, Taratula O, Chem. Mater 2015, 27, 6155.

[39]. Grossen P, Witzigmann D, Sieber S, Huwyler J, J. Controlled Release 2017, 260, 46.

[40]. Steinthorsdottir V, Thorleifsson G, Aradottir K, Feenstra B, Sigurdsson A, Stefansdottir L, Kristinsdottir AM, Zink F, Halldorsson GH, Munk Nielsen N, Geller F, Melbye M, Gudbjartsson DF, Geirsson RT, Thorsteinsdottir U, Stefansson K, Nat. Commun 2016, 7, 12350. [PubMed: 27453397]

[41]. Binétruy-Tournaire R, Demangel C, Malavaud B, Vassy R, Rouyre S, Kraemer M, Plouët J, Derbin C, Perret G, Mazié JC, The EMBO Journal 2000, 19, 1525. [PubMed: 10747021]

[42]. Pineiro-Redondo Y, Banobre-Lopez M, Pardinas-Blanco I, Goya G, Lopez-Quintela MA, Rivas J, Nanoscale Res. Lett 2011, 6, 383. [PubMed: 21711915]

[43]. Yerlikaya G, Balendran S, Pröstling K, Reischer T, Birner P, Wenzl R, Kuessel L, Streubel B, Husslein H, Eur. J. Obstetr. Gynecol. Reprod. Biol 2016, 204, 88.

[44]. Machado DE, Abrao MS, Berardo PT, Takiya CM, Nasciutti LE, Fertil. Steril 2008, 90, 148. [PubMed: 17765237]

[45]. Novella-Maestre E, Carda C, Ruiz-Sauri A, Garcia-Velasco JA, Simon C, Pellicer A, Biol. Reprod 2010, 83, 866. [PubMed: 20574053]

[46]. Brenner RM, Nayak NR, Slayden OD, Critchley HO, Kelly RW, Ann. NY Acad. Sci 2002, 955, 60. [PubMed: 11949966]

[47]. Meduri G, Bausero P, Perrot-Applanat M, Biol. Reprod 2000, 62, 439. [PubMed: 10642585]

[48]. Nayak NR, Critchley HO, Slayden OD, Menrad A, Chwalisz K, Baird DT, Brenner RM, J. Clin. Endocrinol. Metab 2000, 85, 3442. [PubMed: 10999847]

[49]. Zhao MD, Cheng JL, Yan JJ, Chen FY, Sheng JZ, Sun DL, Chen J, Miao J, Zhang RJ, Zheng CH, Huang HF, Int. J. Nanomedicine 2016, 11, 1323. [PubMed: 27099493]

[50]. Franasiak JM, Burns KA, Slayden O, Yuan L, Fritz MA, Korach KS, Lessey BA, Young SL, Reprod. Sci 2015, 22, 442. [PubMed: 25031316]

[51]. Liu Q, Ma P, Liu L, Ma G, Ma J, Liu X, Liu Y, Lin W, Zhu Y, Eur. J. Pharm. Sci 2017, 96, 542. [PubMed: 27989857]

[52]. Sumathi VP, McCluggage WG, J. Clin. Pathol 2002, 55, 391. [PubMed: 11986349]

[53]. Bruner-Tran KL, Mokshagundam S, Herington JL, Ding T, Osteen KG, Curr. Womens Health Rev 2018, 14, 173. [PubMed: 29861705]

[54]. Slayden O, Martin LD, Animal Models in Endometriosis Part-1; Nonhuman Primate Models. Bentham Science Publishers, 2018; Vol. 14, p 8.

[55]. Greenberg LH, Slayden OD, Am. J. Obstet. Gynecol 2004, 190, 1788. [PubMed: 15284801]

[56]. Grummer R, Hum. Reprod. Update 2006, 12, 641. [PubMed: 16775193]

[57]. Awwad JT, Sayegh RA, Tao XJ, Hassan T, Awwad ST, Isaacson K, Hum. Reprod 1999, 14, 3107. [PubMed: 10601104]

[58]. Brenner RM, Rudolph L, Matrisian L, Slayden OD, Hum. Reprod 1996, 11 Suppl 2, 150. [PubMed: 8982757]

[59]. Fritsch M, Schmidt N, Groticke I, Frisk AL, Keator CS, Koch M, Slayden OD, PLoS One 2015, 10, e0142429. [PubMed: 26588841]

[60]. Brenner RM, Nayak NR, Slayden OD, Critchley HO, Kelly RW, Ann. NY Acad. Sci 2002, 955, 60. [PubMed: 11949966]

[61]. Kandala SK, Liapi E, Whitcomb LL, Attaluri A, Ivkov R, Int. J. Hyperthermia 2019, 36, 115. [PubMed: 30541354]

[62]. Rodrigues HF, Capistrano G, Bakuzis AF, Int. J. Hyperthermia 2020, 37, 76.

[63]. Tsuchiya K, Nitta N, Sonoda A, Nitta-Seko A, Ohta S, Otani H, Takahashi M, Murata K, Murase K, Nohara S, Mukaisho K, Int. J. Nanomedicine 2011, 6, 1587. [PubMed: 21845049]

[64]. Gramoun A, Crowe LA, Maurizi L, Wirth W, Tobalem F, Grosdemange K, Coullerez G, Eckstein F, Koenders MI, Van den Berg WB, Hofmann H, Vallee JP, Arthritis Res. Ther 2014, 16, R131. [PubMed: 24957862]

[65]. Rosenblum D, Joshi N, Tao W, Karp JM, Peer D, Nat. Commun 2018, 9, 1410. [PubMed: 29650952]

[66]. Obaidat IM, Issa B, Haik Y, Nanomaterials (Basel) 2015, 5, 63. [PubMed: 28347000]

[67]. Ortega D, Pankhurst Q, Magnetic Hyperthermia, in Nanoscience, Vol. 1, (Ed: O'Brien P), Royal Society of Chemistry, Cambridge, 2013. p 60.

[68]. Hergt J, Dutz S, J. Magnet. Magn. Mater 2007, 311, 187

[69]. Johannsen M, Gneveckow U, Taymoorian K, Thiesen B, Waldofner N, Scholz R, Jung K, Jordan A, Wust P, Loening SA, Int. J. Hyperthermia 2007, 23, 315. [PubMed: 17523023]

[70]. Egea-Benavente D, Ovejero JG, Morales MDP, Barber DF, Cancers (Basel) 2021, 13, 4583. [PubMed: 34572810]

[71]. Kowalczyk M, Banach M, Rysz J, J. Nephrol 2011, 24, 717. [PubMed: 21956770]

[72]. Bashir MR, Bhatti L, Marin D, Nelson RC, J. Magn. Reson. Imaging 2015, 41, 884. [PubMed: 24974785]

[73]. Zhou Z, Yang L, Gao J, Chen X, Adv. Mater 2019, 31, e1804567. [PubMed: 30600553]

[74]. Samani EN, Mamillapalli R, Li F, Mutlu L, Hufnagel D, Krikun G, Taylor HS, Oncotarget 2019, 10, 2282. [PubMed: 31040919]

[75]. https://www.magneticinsight.com/hyper/.

[76]. Tay ZW, Chandrasekharan P, Chiu-Lam A, Hensley DW, Dhavalikar R, Zhou XY, Yu EY, Goodwill PW, Zheng B, Rinaldi C, Conolly SM, ACS Nano 2018, 12, 3699. [PubMed: 29570277]

[77]. Rivera-Rodriguez A, Hoang-Minh LB, Chiu-Lam A, Sarna N, Marrero-Morales L, Mitchell DA, Rinaldi-Ramos CM, Nanotheranostics 2021, 5, 431. [PubMed: 33972919]

[78]. Liu JF, Neel N, Dang P, Lamb M, McKenna J, Rodgers L, Litt B, Cheng Z, Tsourkas A, Issadore D, Small 2018, 14, e1802563. [PubMed: 30286280]

[79]. Paustenbach DJ, Galbraith DA, Finley BL, Clin. Toxicol 2014, 52, 98.

[80]. Finley BL, Monnot AD, Gaffney SH, Paustenbach DJ, J. Toxicol. Environ. Health B. Crit. Rev 2012, 15, 493. [PubMed: 23199219]

[81]. Tvermoes BE, Unice KM, Paustenbach DJ, Finley BL, Otani JM, Galbraith DA, Am. J. Clin. Nutr 2014, 99, 632. [PubMed: 24500148]

[82]. Abdel-Gadir A, Berber R, Porter JB, Quinn PD, Suri D, Kellman P, Hart AJ, Moon JC, Manisty C, Skinner JA, J. Cardiovasc. Magn. Reson 2016, 18, 29. [PubMed: 27153940]

[83]. Cheung AC, Banerjee S, Cherian JJ, Wong F, Butany J, Gilbert C, Overgaard C, Syed K, Zywiel MG, Jacobs JJ, Mont MA, Bone Joint J. 2016, 98-B, 6.

[84]. Song G, Kenney M, Chen YS, Zheng X, Deng Y, Chen Z, Wang SX, Gambhir SS, Dai H, Rao J, Nat. Biomed. Eng 2020, 4, 325. [PubMed: 32015409]

[85]. Shakil MS, Hasan MA, Uddin MF, Islam A, Nahar A, Das H, Khan MNI, Dey BP, Rokeya B, Hoque SM, ACS Appl. Bio. Mater 2020, 3, 7952.

[86]. Lee JH, Jang JT, Choi JS, Moon SH, Noh SH, Kim JW, Kim JG, Kim IS, Park KI, Cheon J, Nat. Nanotechnol 2011, 6, 418. [PubMed: 21706024]

[87]. Sun S, Zeng H, J. Am. Chem. Soc 2002, 124, 8204. [PubMed: 12105897]

[88]. Sun S, Zeng H, Robinson DB, Raoux S, Rice PM, Wang SX, Li G, J. Am. Chem. Soc 2004, 126, 273. [PubMed: 14709092]

[89]. Sabei FY, Taratula O, Albarqi HA, Al-Fatease AM, Moses AS, Demessie AA, Park Y, Vogel WK, Esfandiari Nazzaro E, Davare MA, Alani A, Leid M, Taratula O, Nanomedicine 2021, 37, 102446. [PubMed: 34303840]

[90]. Taratula O, Dani RK, Schumann C, Xu H, Wang A, Song H, Dhagat P, Taratula O, Int. J. Pharm 2013, 458, 169. [PubMed: 24091153]

[91]. Esfandiari Nazzaro E, Sabei FY, Vogel WK, Nazari M, Nicholson KS, Gafken PR, Taratula O, Taratula O, Davare MA, Leid M, Pharmaceutics 2021, 13, 1553. [PubMed: 34683845]

[92]. Duong T, Li X, Yang B, Schumann C, Albarqi HA, Taratula O, Taratula O, Nanomedicine 2017, 13, 955. [PubMed: 27884637]

[93]. Centeno C, Markle J, Dodson E, Stemper I, Williams C, Hyzy M, Ichim T, Freeman M, J. Transl. Med 2018, 16, 246. [PubMed: 30176875]
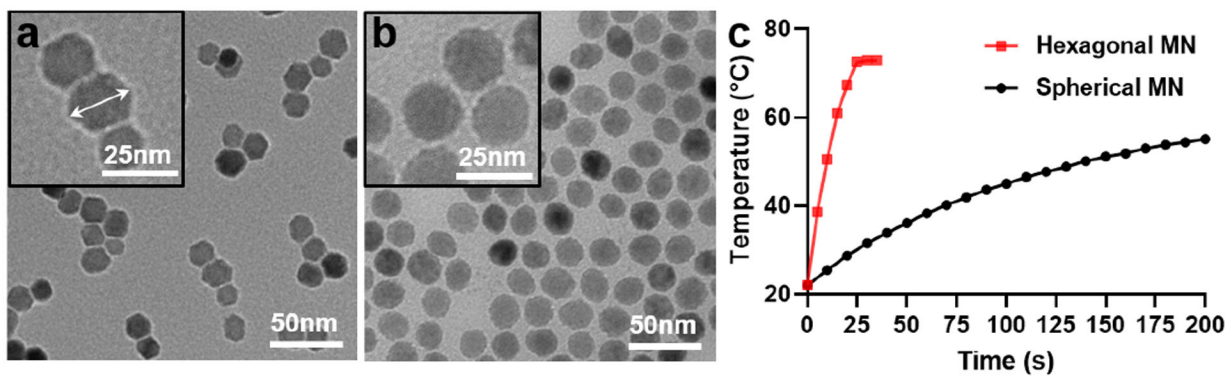
Figure 1.
(a - b) Representative TEM images of Co-doped hexagonal iron oxide nanoparticles **(a)** and spherical iron oxide nanoparticles **(b)**. **(c)** Heating profiles of Co-doped hexagonal magnetic nanoparticles (Hexagonal MN) and spherical iron oxide nanoparticles (Spherical IONP) in tetrahydrofuran (THF) (Fe concentration =1.0 mg mL^{-1}) under AMF (f = 420 kHz, H = 26.9 kA m^{-1}).
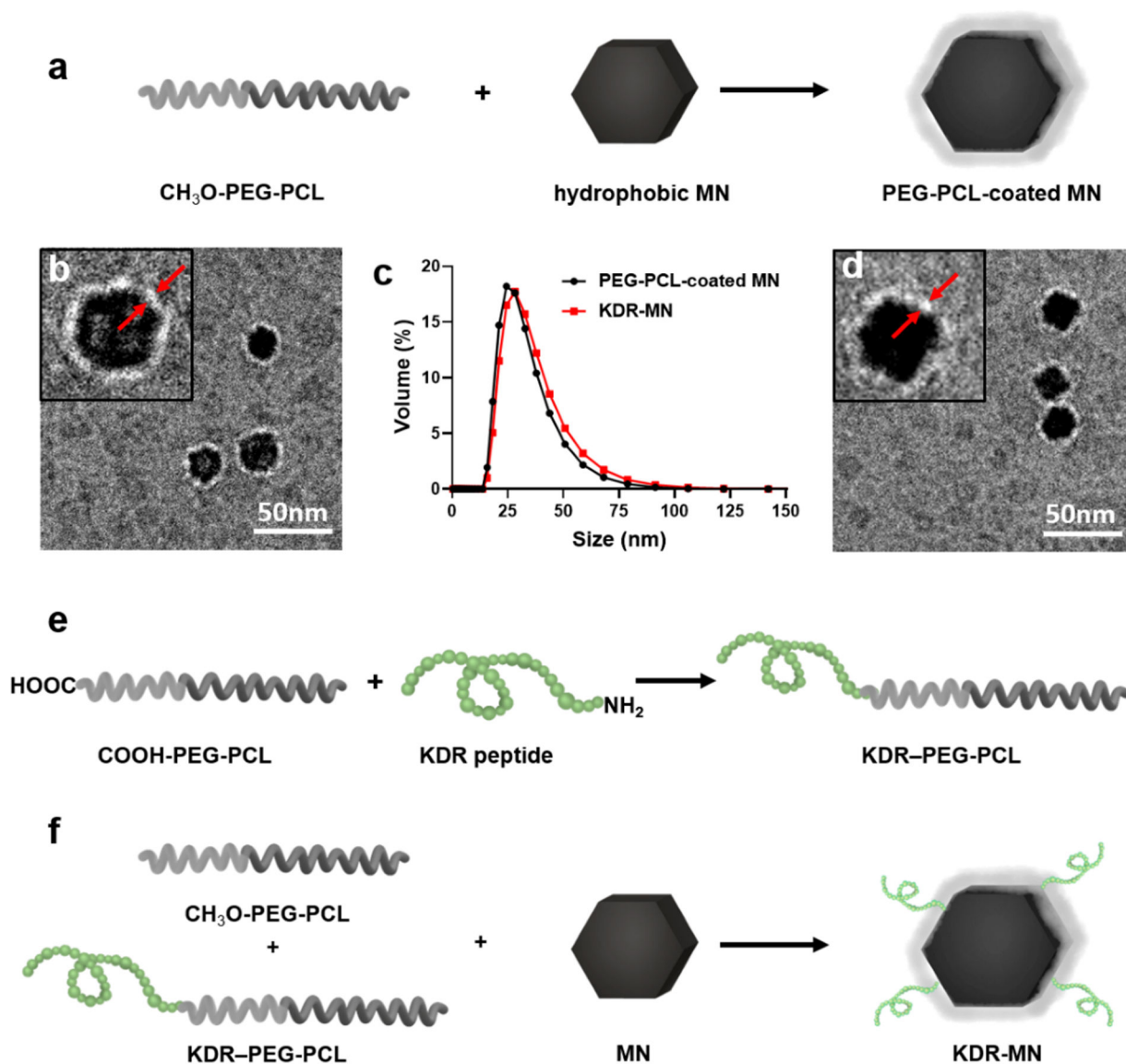
Figure 2.
(a) Schematic illustration of encapsulation of hydrophobic hexagonal magnetic nanoparticles (MN) into PEG-PCL-based polymeric carriers (PEG-PCL-coated MN or non-targeted MN). **(b –d)** Representative cryo-TEM images and dynamic light scattering profiles of non-targeted MN **(b, c)** and KDR-targeted MN **(c, d)**. Red arrows depict the PEG-PCL layer. **(e – f)** Two-step preparation of KDR-targeted magnetic nanoparticles (KDR-MN). Step 1: Conjugation of the KDR peptide to the carboxylic acid-terminated PEG-PCL via an amide bond **(e)**. Step 2: Encapsulation of MN into polymeric carriers consisting of the synthesized KDR-PEG-PCL and CH$_3$O-PEG-PCL **(f)**.
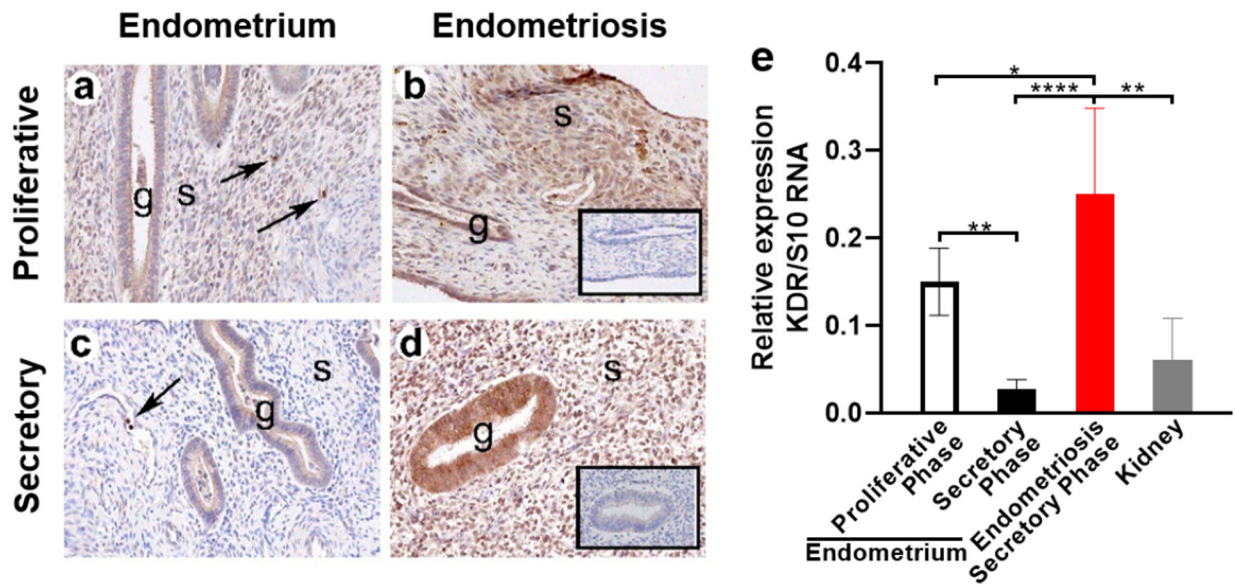
Figure 3.

(a-d) Immunostaining for KDR in macaque eutopic endometrium and endometriosis lesions. KDR staining (brown) is stronger in stroma (S) in endometriosis lesions. Only vascular cells (arrows) show staining in eutopic endometrium. **Inset:** negative control, g=gland. **(e)** qPCR analysis shows the expression of KDR in macaque eutopic endometrium (proliferative (n = 5) and secretory (n = 8) phases), endometriosis lesions (secretory phase (n = 6)), and kidneys (n = 3). Means ± SD are shown. Statistical comparisons among groups were executed using one-way ANOVA. $*p < 0.05$; $**p < 0.01$; $****p < 0.0001$.
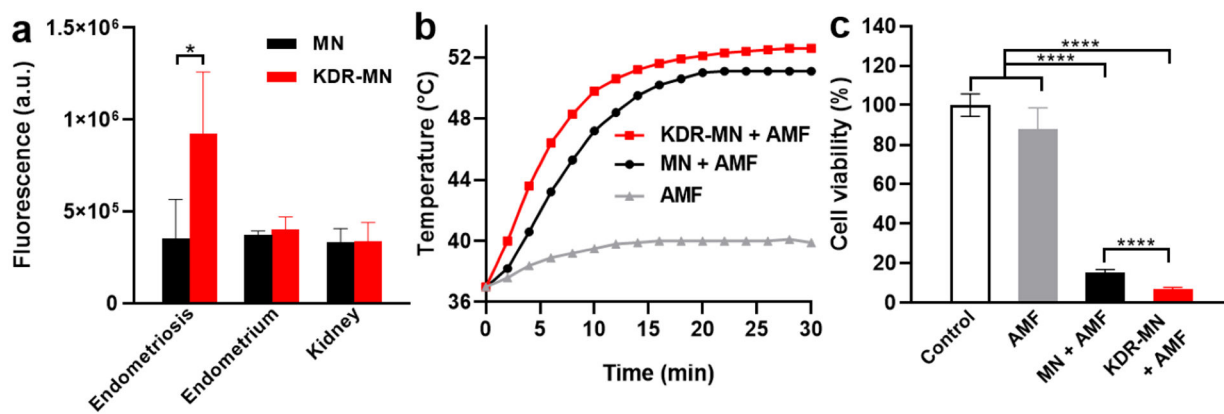
Figure 4.
(a) Flow cytometry analysis of cellular uptake of dye-labeled non-targeted (MN, black bar) and KDR-targeted magnetic nanoparticles (KDR-MN, red bar) by macaque endometriosis stroma cells, endometrium cells and kidney cells after incubation for 24 h. Data shown are means ± SD. The unpaired t-test was used for statistical comparisons. (n = 5, $*p <$ 0.05). **(b)** Temperature profiles of endometriosis cells treated with medium (AMF, gray curve), non-targeted MN (MN + AMF, black curve), and KDR targeted MN (KDR-MN + AMF, red curve) for 24 h at the nanoparticle concentration of 25 μg mL^{-1} Fe and exposed for 30 min to AMF (420 kHz, 26.9 kA m^{-1}). **(c)** Viability of endometriosis cells after the above-indicated treatments. Data shown are means ± SD. Statistical comparisons were performed with one-way ANOVA (n = 20, $****p < 0.0001$).
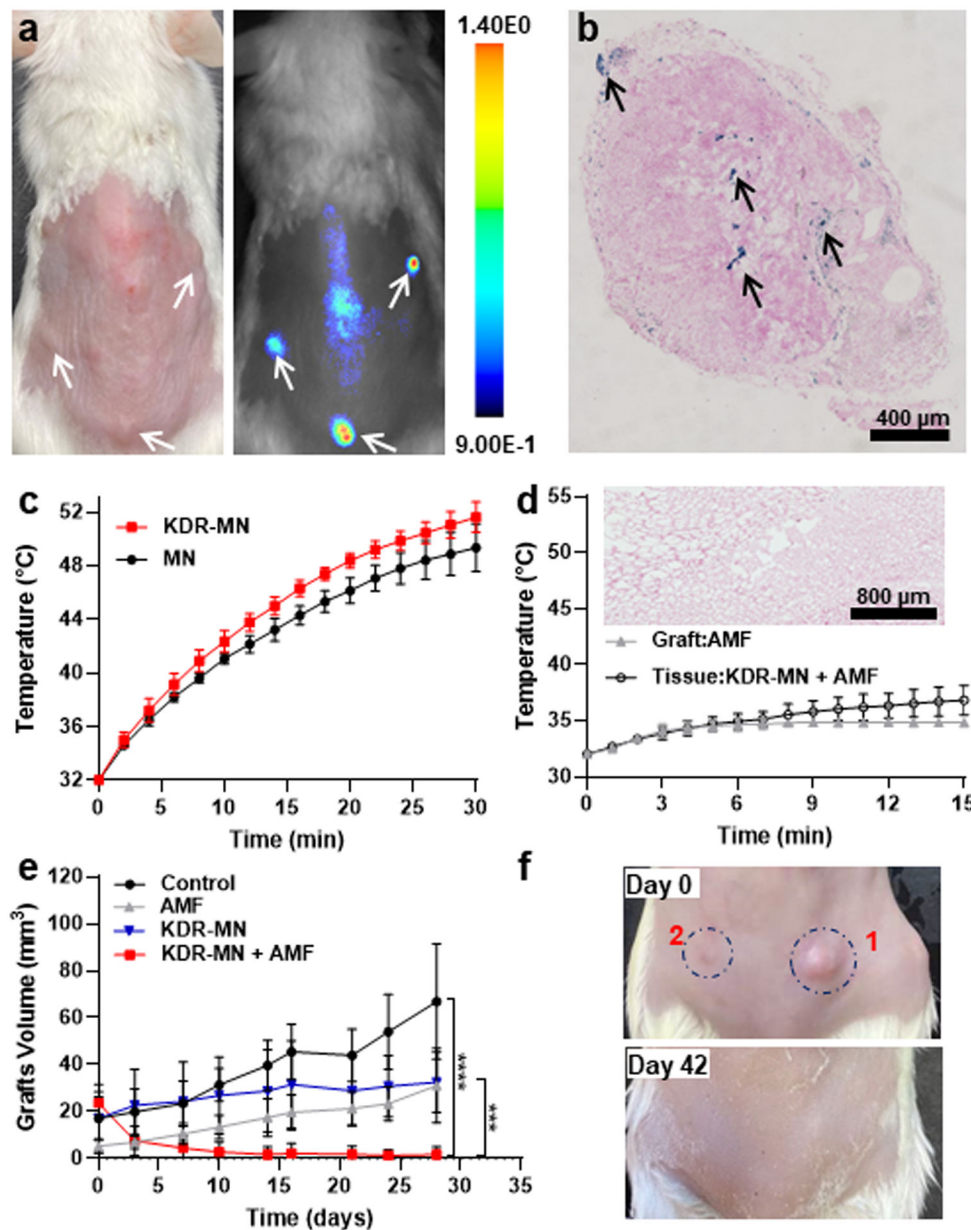
Figure 5.
(a) Representative photograph (left) and NIR fluorescence image (right) of a mouse with multiple endometriotic grafts (white arrows) at 5 days after IV injection of KDR targeted MN (3 mg Fe per kg) loaded with a NIR fluorescence dye (SiNc). (b) Representative Prussian blue stained (black arrows) section of an endometriotic graft collected from a mouse at 5 days post-injection with KDR-MN. (c) Temperature profiles inside of endometriotic grafts during AMF (420 kHz, 26.9 kA m^{-1}) exposure at 5 days after IV administration of non-targeted MN (3 mg Fe per kg, n = 3) and KDR-MN (3 mg Fe per kg, n = 3). (d) Temperature profiles of endometriotic grafts (grey curve, Graft: AMF) and tissues adjacent to grafts (black curve, Tissue: KDR-MN + AMF). Prior to AMF exposure, mice were IV injected with a single dose of saline (Graft: AMF, n = 3) or KDR-MN (3 mg

Fe per kg, Tissue: KDR-MN + AMF, n = 3). Mice were subjected to AMF at 5 days after nanoparticle injection. **Inset:** Prussian blue staining of tissue adjacent to a graft resected from a mouse at 5 days post-injection with KDR-MN. **(e)** Growth curves of grafts after the following treatments: (i) Control: mice were IV injected with saline (n = 4); (ii) AMF: mice were injected with saline and exposed to AMF for 20 min (n = 4); (iii) KDR-MN: mice were IV injected with KDR-MN (3 mg Fe per kg, n = 4); (iv) KDR-MN + AMF: mice were IV injected with KDR-MN (3 mg Fe per kg) and subjected to AMF for 20 min at 5 days post-injection (n =5). Data shown are means ± SD. Statistical comparisons between groups were performed with one-way ANOVA (***$p < 0.001$, ****$p < 0.0001$). **(f)** Photographs of a mouse bearing two endometriotic grafts (20 mm^3 and 2 mm^3) before and 42 days after a single hyperthermia treatment.
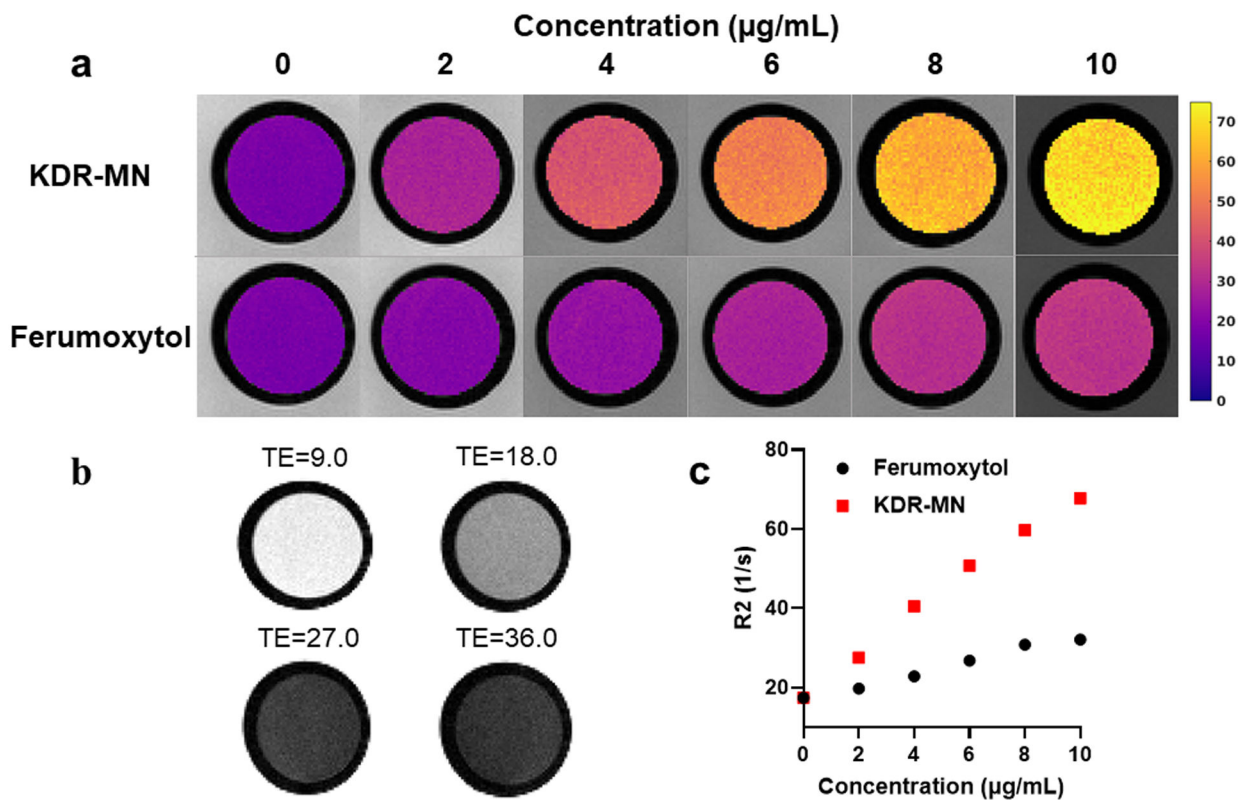
Figure 6.
In vitro T2-weighted and R2 relaxation rates for magnetic resonance imaging of nanoparticle solutions. **(a)** R2 relaxation rate maps of KDR-MN solutions of various concentrations compared to R2 relaxation rate maps of ferumoxytol solutions (in units of 1/s). **(b)** Four echo (TE) images acquired in the KDR-MN solution (8 μg mL^{-1}) demonstrating progressive signal dropout of KDR-MN with increasing TE. **(c)** Plot of R2 relaxation rates for KDR-MN and ferumoxytol solutions at various concentrations.
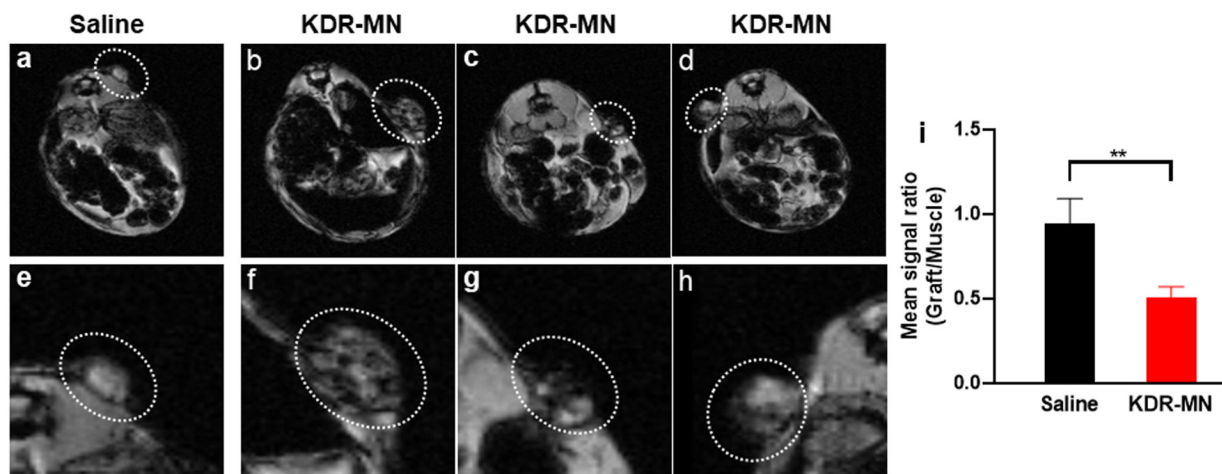
Figure 7.
T2-weighted magnetic resonance images (MRI at TE 4.5 milliseconds) were obtained after 24 h in mice injected intravenously with (**a** and **e**) saline and (**b - d** and **f - h**) KDR-MN (3 mg Fe per kg). **e - h** are magnified images of **a - d**. Note the relatively darker signal in the endometriosis graft with the KDR-MN injected mouse, showing localization of the nanoparticles by MRI and its property as a negative contrast imaging agent. (**i**) The mean signal ratio between grafts is normalized to skeletal muscle (internal control) in mice injected with saline (n = 3 grafts) and KDR-MN (n = 3 grafts). Data shown are means ± SD. The unpaired t-test was used for statistical comparisons (**$p < 0.01$).

Figure 8.
Photographs of a mouse bearing two macaque endometriotic grafts before and 23 and 32 days (no skin) after single hyperthermia treatment. This mouse was IV injected with KDR-MN (3 mg Fe per kg) and only lesion #1 was exposed to AMF for 20 min on day 5 post-injection.
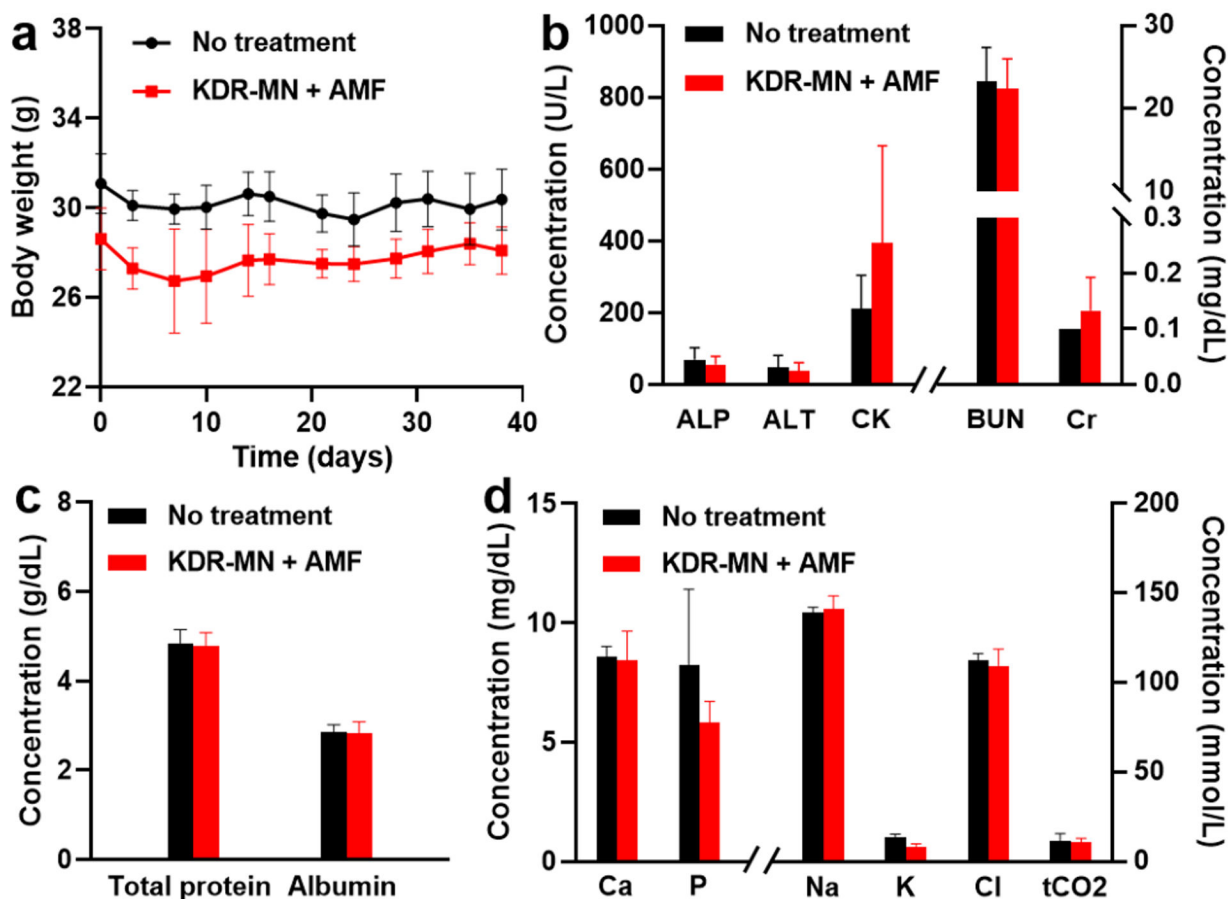
Figure 9.
(a) Body weights of mice injected with saline (no treatment, n = 4) and mice treated with magnetic hyperthermia (KDR-MN + AMF, n = 5). **(b – d)** Serum levels of biomarkers, proteins and electrolytes in non-treated mice and mice exposed to magnetic hyperthermia. Serum samples were collected 42 days after the treatment. Data shown are means ± SD.